Structural fibre-reinforced cement-based composite designed for particle bed 3D printing systems. Case study Parque de Castilla Footbridge in Madrid

A. de la Fuente [a,*], A. Blanco [b], E. Galeote [a], S. Cavalaro [b]

[a] Department of Civil and Environmental Engineering, Universitat Politècnica de Catalunya, Jordi Girona 1-3, 08034 Barcelona, Spain
[b] School of Architecture, Building and Civil Engineering, Loughborough University, Loughborough, Leicestershire LE11 3TU, United Kingdom

ARTICLE INFO

ABSTRACT

This paper presents the material and process-related research that underpinned the realisation of the Parque de Castilla Footbridge in Madrid in 2016, going from the laboratory to the industrial scale. The fibre-reinforced cement-based composite was first developed and tested in a small-scale particle bed printer focusing on evaluating the influence of the material and process on the mechanical response and density of the printed parts. The solution was then upscaled to a full-size particle bed printer that underwent technical modifications to ensure adequate control and production quality of the footbridge segments. The observations derived from the study provide valuable insights on relevant process-related differences induced by the technology upscaling that can inform future applications of the technology.

1. Introduction

In recent years, substantial progress has been made regarding the adaptation and use of additive manufacturing (AM) processes to produce infrastructure components [1]. Research groups around the world have worked to understand the implications of the new production approaches from the process [2,3], material [4,5] and structural standpoints [6]. The interest has grown notably in those methods deploying mixes with Portland-cement [7], although automation has been applied with other building materials such as stone [8] and earth [9].

Different AM methods have been developed to enable digital fabrication with concrete (DFC). Buswell et al. [10] presented a comprehensive review of these methods, their limitations and potential fields of application. The same authors also proposed a process classification framework based on seminal work from the RILEM technical committee 276-DFC on "Digital fabrication with cement-based materials". The classification includes three main groups depending on the strategy adopted for the deposition of the Portland cement-based material: particle bed binding, material extrusion and material jetting. Please refer to [10] for more information about these groups.

Analysing the number of AM research papers published in the past ten years applied to construction shows that studies have focused predominantly on extrusion rather than particle bed [16]. A similar

conclusion arises from quantifying real-life industrial applications to produce large-scale construction components or structures, where the particle bed systems lag behind extrusion-based ones. Such interest disparity reflects the scientific and technical communities' perception around the more limited breadth of potential applications, the more significant challenges of setting up the machinery required in the laboratory and, in particular, the potentially more complex upscaling to an industrial level of particle bed 3D printing systems.

Lowke et al. [11,12] identifies three types of particle bed 3D printing systems. In the selective binder activation type, a particle bed made of a dry mixture of fine aggregate and binder is activated in defined areas via the selective deposition of an activator that reacts with the binder and allows it to set [13]. In the selective paste intrusion type, a paste made with a binder and activator is selectively distributed over a solid particle bed [14]. In the binder jetting type, the binder is injected into a bed with aggregate and activator [15]. Most academic work about these technologies is based on experimental programs with small printers. To the authors' best knowledge, no published work has bridged the gap between small-scale research and large-scale industrial application, highlighting relevant process-related differences induced by the technology upscaling.

Aside from interesting conceptual developments for the construction of lunar bases [18], possibly the most emblematic and earliest real-life

---

successful application of the binder activation approach for infrastructure construction is the footbridge built by ACCIONA at the Parque de Castilla (Alcobendas, Madrid) in 2016, which was based on the D-shape technology developed by Enrico Dini and used the design from IAAC [11,19]. This footbridge represents a clear milestone and an example of the potential applications of particle bed 3D printing systems and the significance of DFC for the construction industry.

Despite this achievement, more work is still required to develop further and build sufficient technical confidence around applying particle bed 3D printing approaches [17]. This paper aims to present the material research and process-related findings that supported and led to the construction of the footbridge, going from the small laboratory to the large industrial scale. The results included here shed light on how relevant anisotropic mechanical properties are affected by the composition of the material and process-related aspects. This, combined with the description of the footbridge production and construction, highlight some of the challenges facing the future technology uptake for the production of structural components. This work was framed in the context of a series of R&D projects between ACCIONA, S.A., the Polytechnic University of Catalonia (UPC, BarcelonaTECH) and Smart Engineering (Spin-off, UPC).

2. Small-scale particle bed system

A small-scale particle bed system was developed to produce the samples in the laboratory. The purpose was to identify the material (binder type and amount, w/c ratio, fibre type and content) and production parameters (environmental conditions, water temperature, activator pressure, layer compaction and height) that govern the mechanical performance of the hardened cementitious composite. The design of the printing system was simplified by introducing manual elements (i.e., compaction) that would usually be automated. Aside from that, the production process is the same as in a real-scale particle bed system. Fig. 1a shows the small-scale printer and its main components: a support tray, the box where the specimen is manufactured, a platform that moves vertically, a hopper for the solid material, a pressure tank for the liquid, an electric board, a system of electro valves and a microprocessor.

The hopper and electro valve system are displaced forwards and backwards using a set of pistons mobilised by a 3.5-bar air compressor. The displacement speed was controlled by regulating the air intake. The liquid activator is placed in a tank connected to the compressor to adjust the water outlet pressure between 0.1 and 0.2 bar. The tank is connected through hoses to 10 electrovalves or injectors placed on top of the printing head (see Fig. 1b), which moves along the printing box and distributes the liquid activator. The microprocessor placed in the electric board controlled the state of the electrovalves (i.e., open or closed) when the printing head moved.

3. Experimental program

3.1. Materials, mixes and production

Fourteen mix proportions were produced with the small-scale 3D printer using the mix proportions in Table 2. They contained Portland cement (CEM I 52.5 R), limestone sand, filler, superplasticiser (GLENIUM ACE 456, in liquid form), water at ambient temperature (18–22 °C) and 70 °C and fibres (either metallic, polymeric or PVA, with characteristics as per Table 1).

The fibre contents by the total volume of materials equate to 1.3% for metallic, 1.0% and 1.3% for polymeric and 1.0% and 1.8% for the PVA fibres. These contents were selected based on previous experiences of the authors on both the design, and mechanical performance of fibre reinforced components [20–22] with similar requirements in terms of post-cracking flexural performance as those targeted for structural applications by ACCIONA. The layer thickness depends on the compaction method used [11,12]. Based on internal discussions, layer thicknesses of 5 and 7 mm before compaction were adopted in this experimental program.

The notation used to identify the specimens and the corresponding mix consist of four groups of characters separated by hyphens. The first group of characters corresponds to the concrete batch. Batches sharing the same mix proportions were indicated by their range (e.g., 11to14 – meaning batch 11 to batch 14). The second group of characters refer to the fibre type ('M' for metallic, 'P' for polymeric polypropylene and 'A' for polymeric PVA). Notice that P and A are followed by a number indicating the fibre content as more than one content was used for polypropylene and PVA fibres. The third group of characters in the notation refers to the cement content (7 for high and 5 for low content), followed by 'f' if the mix contained filler or 'a' if the mix contained sand 0/1. No letter was appended to mixes without additional fines. The last group of characters refers to the initial thickness of the layer (either 5 or 7 mm), the compaction energy applied to each layer ('L' for low energy and 'I' for intense energy, as per the description of the compaction procedure below) and the flexural testing setup as per Fig. 3. For example, mix 7-M-7-7LX indicates batch 7, produced with metallic fibres [M] and high (528 kg/m^3) cement content (7). This mix does not contain additional fines since the cement content is not followed by any

Table 1
Characteristics of the fibres.

Characteristics	Metallic [M]	Polymeric [P]	Polymeric (A)
Commercial brand	Dramix OL 13/0.16	Masterfiber 240	Masterfiber 400
Material	Steel	100% Polypropylene	100% PVA
Tensile strength (N/mm^2)	3000	338	790
Length (mm)	13	40	12
Diameter (mm)	0.15	0.75	0.16–0.24
Aspect ratio	87	53,3	75–50

Fig. 1. a) Small-scale particle bed system and b) printer head with 10 electrovalves or injectors.

letter (f or a). Finally, the height of the layers is 7 mm, which was compacted using low energy (L). Specimens from this batch were subject to the flexural test setup X.

The mix 1-M-7f-7LX was taken as a reference, and all others resulted from modifications in the proportions to achieve acceptable water penetration and strength performance. The iterative process followed to develop mixes viable for printing and testing is described in detail in the following section 'Preliminary Results and Adjustment of the Mixes'.

Two possible philosophies were considered to represent the composition of the mixes: to use the content in kg/m³ or the relative weight of components presented together with the density after compaction. Both are given in Table 2, although the latter was deemed more practical for industrial applications. By defining the compositions in terms of the weight in relation to the cement content, the proportion by weight between solid materials is kept constant regardless of the final density achieved. If the total weight of dry solids placed in each layer is known, the weight of water to be distributed over this layer can be calculated using the proportion between the activated area and the total area where the solids were distributed. This can be easily converted into a water flow depending on the translational speed of the printing head. Regarded the water exchange with inactivated parts is limited, and the part size is several times bigger than the layer thickness, the w/c ratio should be nearly the same throughout the part for any final density.

First, the liquid activator (regular water from the supply system) content was calibrated for each mix by weighing the water output when the printing head moved forward and backwards. Notice that the irrigated area when the printing head moved forward did not coincide with the area irrigated when the printing head moved backwards. Hence, there was an effective printing area (see Fig. 2a) that limited the dimensions and number of specimens produced per batch.

After the calibration, the solid components were mixed and distributed with a hopper over the printing bed. The samples were produced by uniformly distributing the solid components with the hopper in a layer (see Fig. 2c) that was then manually compacted using a weight of 1.54 kg for batches 1 to 8 and 2.55 kg from batch 9 onwards after detecting

that the compaction was insufficient. The weight was applied either in a static (low energy) or a dynamic (high energy) manner. Subsequently, the print head was activated, and the electro valves release the liquid activator when it moved forward and backwards (see Fig. 2d). This procedure was repeated until the desired height of the sample was reached. In this study, the target height for the sample was 80 mm. The sample was removed from the mould 24 h after printing (see Fig. 2b).

The specimens were stored in a curing room at 20 ± 1 °C and 95% relative humidity until cutting (after 7 days of curing). The coordinated system in Fig. 3a was adopted to identify the direction of extraction of the specimens. The X-axis is contained in the horizontal plane and is parallel to the displacement of the printing head. The Y-axis is also contained in the horizontal plane and is perpendicular to X. The Z-axis is vertical. The samples were cut into beams (40 × 40 × 160 mm) with their biggest dimensions parallel to X, Y or Z (as shown in Fig. 3a, b and c, respectively). After cutting, one in every three specimens were tested, and the others continued the curing (one of them submerged in water at 20 °C and the other in a curing room at 20 ± 1 °C and 95% relative humidity). All specimens were removed from the curing regime 24 h before the mechanical tests. Fig. 3 also depicts the alignment of the printing layers and the 4 flexural test setups depending on the cracking plane created during this test.

3.2. Testing methods

The flexural strength, compressive strength and modulus of elasticity were characterised. The configurations of the flexural and compressive strength tests were based on UNE-EN 1015-11:2000/A1:2007 [23] (now superseded by UNE-EN 1015-11:2020 [24]). However, the loading procedure did not follow the stages gathered in the standard to maximise the information collected and account for the presence of fibres. During the 3-point bending test (3PBT), the machine crosshead moved at a rate of 0.08 mm/min up to 0.2 mm of displacement and 0.21 mm/min to the end of the test at 4 mm of displacement. The load was applied in one of the two smooth surfaces of the beam generating a crack in the bottom

Table 2

Process parameters and mix proportions (values outside the parenthesis give the weight ratio in relation to cement, whereas values in parenthesis show the estimated content in kg/m³).

Notation	Cem	Filler	Sand 0/1	Sand 0/2	Water	Water 70 °C	Fibre (Type)	w/c	Layer thick[a] (mm)	Comp. energy[b]	Load direction
1to4-M-7f-7LX	1 (485)	0.79 (381)		1 (485)	0.25 (121)		0.14 (69) [M]	0.25	7	L	X
5to6-M-7-7LX	1 (518)			1.79 (925)	0.25 (129)		0.14 (74) [M]	0.25	7	L	X
7-M-7-7LX	1 (528)			1.79 (943)		0.25 (132)	0.14 (75) [M]	0.25	7	L	X
8-M-7f-7LX	1 (557)	0.14 (80)		1.64 (915)	0.25 (139)		0.14 (80) [M]	0.3	7	L	X
9-M-5a-7LX	1 (387)		0.4 (155)	2.5 (966)		0.35 (135)	0.2 (77) [M]	0.35	7	L	X
10-M-5a-5LX	1 (414)		0.4 (166)	2.5 (1036)	0.5 (207)		0.2 (83) [M]	0.5	5	L	X
11to14-M-5a-5IX	1 (454)		0.4 (182)	2.5 (1134)	0.42 (191)		0.2 (91) [M]	0.42	5	I	X
15-M-5a-5IY	1 (465)		0.4 (186)	2.5 (1163)	0.42 (195)		0.2 (93) [M]	0.42	5	I	Y
16-M-5a-5IX	1 (385)		0.5 (193)	3.13 (1205)	0.43 (164)		0.25 (96) [M]	0.42	5	I	X
18-P12-5a-5IX	1 (470)		0.4 (188)	2.5 (1176)	0.42 (198)		0.02 (11) [P]	0.42	5	I	X
19-P9-5a-5IX	1 (471)		0.4 (188)	2.5 (1177)	0.42 (198)		0.02 (8) [P]	0.42	5	I	X
20-A22-5a-5IX	1 (485)	0.79 (381)		1 (485)	0.25 (121)		0.14 (69) [M]	0.42	5	I	X
21-A12-5a-5IX	1 (518)			1.79 (925)	0.25 (129)		0.14 (74) [M]	0.42	5	I	X
22-M-5a-5IZ	1 (528)			1.79 (943)	0 (0)	0.25 (132)	0.14 (75) [M]	0.42	5	I	Z-ZX

[a] Layer thickness before compaction.
[b] Manual compaction using a weight of 1.54 kg and 2.55 kg in a static (low energy) or dynamic (high energy) manner.

Fig. 2. a) and b) Effective surface of irrigation, c) distribution of solid components, and d) irrigated surface.
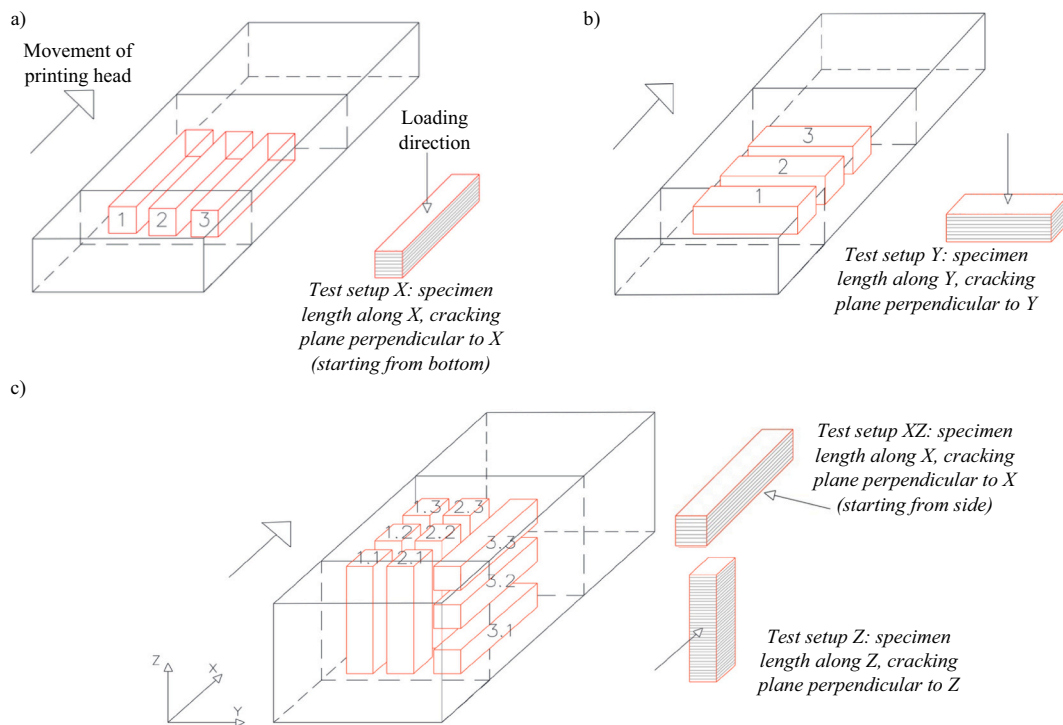

Fig. 3. Cutting and testing direction for the beams.

surface, usually close to halfway through the span (see Fig. 4a). The 2 halves of the beam obtained were separated from each other and tested in compression (see Fig. 4b). The compressive tests were performed with a crosshead displacement control at a 5 mm/min rate and with load application at an area of 40 × 40 mm.

The modulus of elasticity was characterised according to EN 12390-13 [25] (Method B) by performing a uniaxial compression test with compressive stress cycles (see Fig. 4c). Three prismatic specimens with a 40-mm square cross-section and 80-mm of length (slenderness 2) were cut with the length parallel to the printing direction. The specimens

Fig. 4. a) 3-point bending test, b) compressive test and c) setup for assessment of elastic modulus.

were placed with the longer side vertical and perpendicular to the plates of the testing machine. Three linear variable differential transformers (LVDT) with a range of 5 mm were used to measure the displacement. The secant modulus of elasticity value was obtained according to the standard.

4. Preliminary results and adjustment of the mixes

In the absence of mix design guidelines and experience with the small-scale particle bed printer, batches 1 to 6 in Table 2 were produced to collect information about the production process, testing procedure and mechanical behaviour expected with different fibre types. These mixes were then iteratively adjusted to overcome the issues observed during printing, testing or after the analysis of the results.

The first four batches (see 1 to 4-M-7f-7LX in the first line of Table 2) served to determine the correct setup of the small-scale particle bed system and establish a suitable procedure for manufacturing and extracting the beams for the tests. During the execution of batches 1 to 3, the distribution of the solid material with the hopper was optimised to achieve a layer thickness of approximately 7 mm. Visual observations of the printing process showed a slow penetration of the liquid activator. Fig. 5 illustrates the compacting (Fig. 5a), the penetration of the reactive agent (Fig. 5b) and the final element (Fig. 5c).

The printing layers were visible at the specimens' sides after cutting, indicating significant heterogeneity and potentially poor interlayer connection (see Fig. 6a). In a few specimens, the bond between layers was not sufficiently strong to withstand the movement of the saw during the cutting process, which led to the separation between layers and loss of integrity. Two circular saws were used after that to overcome the difficulties found in the cutting procedure and improve the finishing of the beams. The printed sample was cut with a less accurate saw in three smaller elements, then cut into the specimens with a smaller and more precise circular saw. The mechanical performance of the beams manufactured with these early batches was significantly below the authors' expectations. A closer visual inspection of the specimens suggested that part of the layers seemed not fully hydrated (see Fig. 6b), thus suggesting a non-uniform water distribution. The authors suspected this finding could be linked to an excessive amount of filler in the mixes that created a denser packing and compromised the water penetration over

the layer depth.

To verify this hypothesis, the authors printed 3 layers with the same mix as before and repeated the process with a mix in which the full filler content was substituted by aggregate 0/2. The water penetration and the formation of layers were evaluated visually in both instances. The mix with filler showed the same water penetration issues mentioned earlier whereas the mix without filler presented more uniform hydration and nearly no visual distinction between adjacent layers. Based on this finding, two additional batches (5 and 6) were produced using the mix M-7-7LX that ensured more uniform hydration across the layers. Although the penetration of the reactive liquid seemed acceptable in both batches, some of the specimens were damaged during the cutting process due to insufficient bond between adjacent layers. In some cases, debonding was also detected while testing the specimens under flexure and compression. The average compressive and flexural strength of batches 5 and 6 were 10 MPa and 2.5 MPa, respectively. Both were below the expected performance. This outcome was attributed to the low density of the beams, which were in the order of 1600 kg/m^3 and the lack of internal cohesion detected in the beams.

To ascertain whether the temperature of the water influences the results, batch 7-M-7-7LX was produced using water at 70 °C. During the production, the penetration and distribution of the reactive liquid were satisfactory, leading to visually uniform layer hydration (confirmed after cutting the element into beams). However, there was still insufficient internal cohesion (see Fig. 6c). Batch 8-M-7f-7LX received a slight increment in the content of fines and the addition of 7% by cement weight of superplasticiser (the superplasticiser was mixed with the water before printing). The filler was added to improve the cohesion and the superplasticiser to evaluate any positive influence in the liquid activator penetration. However, the addition of the superplasticiser increased the viscosity of the reactive agent, thus reducing the penetration of the activator. The inclusion of filler had a positive effect on the density (1770 kg/m^3) and the cohesion of the material (Fig. 6d). The improvement was also noticeable in the average flexural and compressive strength that reached 4.48 and 15.85 MPa, respectively.

In batch 9-M-5a-7LX, the filler was substituted by a bigger content of sand 0/1 (finer than the sand 0/2 used up to this point). Such modification sought to increase the content of fines smaller than 1 mm without compromising the penetration of the liquid activator. Moreover, the

Fig. 5. Production process: a) compaction, b) penetration of the reactive agent, and c) final element.

Fig. 6. a) Layers in the cut surface of the beam, b) cross-section of a beam showing non-uniform hydration, c) beam from batch 7-M-7-7LX, d) beam from batch 8-M-7f-7LX, e) beam from batch 10-M-5a-7LX, and f) layer with roughness to improve the bond.

cement content was reduced, and the w/c increased to promote water penetration through the layers (see Table 2). The target thickness was reduced from 7 to 5 mm, and the static weight applied during compaction increased to 2.55 kg to try and improve the bond between layers and the internal cohesion. The mechanical test results were like those obtained for 8-M-7f-7LX while using significantly less cement. Moreover, no debonding between layers was observed, thus, making this the reference mix for the next series of batches. By reducing the thickness of the layer and using a bigger static weight (2.55 kg), the material density increased to 1900 kg/m³. Consequently, the material was visibly more compact and uniform (see Fig. 6e). The average flexural and compressive strength rose to 6.3 MPa and 20.0 MPa, respectively.

The subsequent batch, 10-M-5a-7LX, was produced following the procedure described above but with a w/c that increased from 0.35 to 0.50. The solid particles could not retain the liquid activator, leading to free water. This hindered the compaction and formation of the layers and delayed the penetration of the reactive agent. Due to the excess of water in the previous batch, the w/c was reduced from 0.50 to 0.42 in batch 11-M-5a-7IX. To ensure proper compaction, the process was modified from static to dynamic compaction, which translates into more compaction energy applied to each layer with a weight of 2.55 kg. During the compaction of the layers, it was observed that the liquid activator in the lower layers wetted the upper layers, thus improving their connectivity. Owing to the additional compaction energy, the density of the material reached an average of 2050 kg/m³, and the

beams yielded the best mechanical performance so far with a compressive strength of 36.0 MPa and flexural strength of 9.1 MPa. The visual inspection of the beam revealed better finishing, less porosity and no clear sign of layer debonding.

To improve the interaction between layers, an additional step was included in producing the elements of batch 12-M-5a-7IX. The step consisted in combing the layers after the compaction and deposition of the liquid activator to induce roughness and improve interlayer bond (the penetration of the comb was approximately 1 mm, see Fig. 6f). The average density for this batch was also 2050 kg/m³; nevertheless, the mechanical performance increased noticeably. The compressive strength obtained for 12-M-5a-7IX was 42.0 MPa, and the flexural strength was 7.7 MPa. Based on these results, it was established that the mix proportion and manufacturing method of 12-M-5a-7IX were the most suitable. To confirm the results, two additional batches 13 and 14-M-5a-7IX were produced in the same manner, yielding compressive strength of 49.0 MPa and 48.6 MPa, respectively, and flexural strength of 8.5 MPa and 8.7 MPa, respectively. All subsequent batches were produced according to the procedure adopted for 12-M-5a-7IX. Slight changes to evaluate the influence of different variables such as the cutting direction, fibre type and content.

5. Results and discussion

Table 3 summarises the oven-dry density and the mechanical

Table 3
Mechanical properties of the beams at 28 days.

Beam	Flexural strength (MPa)	Average flexural strength (MPa)	Average compressive strength (MPa)	Average compressive strength per batch (MPa)	Oven-dry density (kg/m^3)	Average density (kg/m^3)
9.2-M-5a-7LX	3.78	4.06	10.8	10.40	1715	1734
9.3-M-5a-7LX	4.33		9.99		1753	
10.2-M-5a-5LX	6.64	6.03	22.66	20.72	1958	1906
10.3-M-5a-5LX	5.41		18.78		1854	
11.2-M-5a-5IX	9.24	9.05	38.31	39.85	2051	2056
11.3-M-5a-5IX	8.86		41.39		2061	
12.1-M-5a-5IX	6.45	7.61	39.33	40.32	1983	2023
12.3-M-5a-5IX	8.76		41.3		2063	
13.2-M-5a-5IX	8.77	8.36	49.61	49.09	2067	2057
13.3-M-5a-5IX	7.94		48.57		2047	
14.2-M-5a-5IX	8.27	8.27	59.31	59.31	2069	2069
15.2-M-5a-5IY	8.23	8.14	43.22	45.79	2110	2102
15.3-M-5a-5IY	8.05		48.35		2094	
16.2-M-5a-5IX	8.19	7.30	33.22	29.77	2070	2043
16.3-M-5a-5IX	6.41		26.32		2015	
18.2-P12-5a-5IX	6.50	6.24	21.57	20.57	1931	2043
18.3-P12-5a-5IX	5.97		19.57		1918	
19.2-P9-5a-5IX	7.36	6.62	22.26	20.73	1926	2043
19.3-P9-5a-5IX	5.87		19.19		1907	
20.1-A22-5a-5IX	5.25	4.49	20.68	24.20	1942	1940
20.2-A22-5a-5IX	4.31		29.25		1951	
20.3-A22-5a-5IX	3.92		22.67		1928	
21.1-A12-5a-5IX	3.42	4.13	25.03	26.97	1913	1956
21.2-A12-5a-5IX	4.43		32.85		2004	
21.3-A12-5a-5IX	4.55		23.04		1952	
22-1.1-M-5a-5IZ	2.98	3.25	27.29	30.45	1913	1950
22-1.2-M-5a-5IZ	3.21		31.02		1985	
22-1.3-M-5a-5IZ	3.55		33.04		1952	
22-2.1-M-5a-5IZ	4.73	4.98	34.7	35.95	2079	2060
22-2.2-M-5a-5IZ	4.52		38.55		2031	
22-2.3-M-5a-5IZ	5.70		34.59		2069	
22-3.1-M-5a-5IZX	7.55	8.78	31.01	33.71	2046	2066
22-3.2-M-5a-5IZX	8.99		34.57		2074	
22-3.3-M-5a-5IZX	9.8		35.56		2077	

properties of all beams tested at 28 days. A number was appended after the batch to identify each beam tested (e.g., 9.2-M-5a-7LX, corresponds to beam 2 of batch 9). For brevity, beams tested at an age other than 28 days are not included in this table; however, they will be used in subsequent graphs and analyses. Note that, in some cases, it was not possible to perform the compression test due to the state of the halves of the beam after the flexural test. The results were analysed according to layer thickness, compaction energy, cutting direction, and curing conditions.

Fig. 7 shows the flexural and compressive strengths and the density of beams cut from batches 9 and 10 (with low compaction energy and containing metallic fibres). The beams manufactured with 5 mm-thick layers exhibited average flexural and compressive strength values up to 48% and 99% bigger than those for equivalent specimens produced with 7 mm-thick layers. A 10% density increment was also observed in the specimens with 5 mm-thick layers. The density is affected mainly by the compaction level, the water surface tension and distribution [11,12],
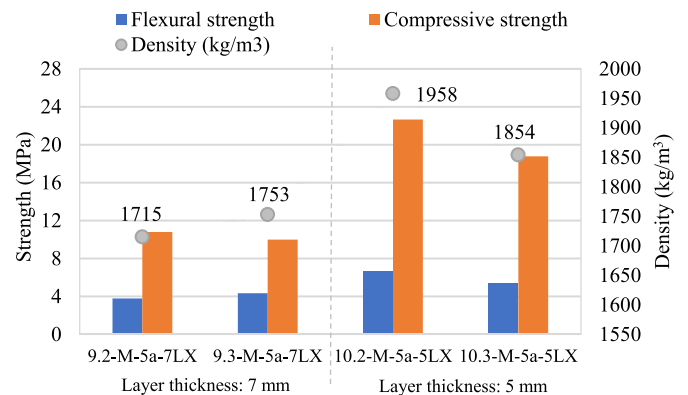

Fig. 7. Influence the layer thickness on beams compacted with low energy.

adsorption onto the particle surfaces and capillary forces [26]. All other aspects remaining constant in those batches, the cause of the density increase should be the change in the compaction level. The reduction in layer thickness from 7 to 5 mm increases the specific compaction energy per unit of material weight. This translates into more compaction, bigger density and improved mechanical performance.

Significant performance differences were also observed when comparing batches produced with the low and high energy compaction. Fig. 8 shows the average flexural and compressive strengths for the 2 compaction processes deployed in the experimental program. Batches subject to intense compaction energy presented a matrix with an average density 10% higher than those compacted using low energy. The average flexural and compressive strengths of the beams compacted intensely are 37.5% and 126% higher than for beams with insufficient compaction, respectively.

Fig. 9a presents the flexural strength for beams testes with setups X, Y, Z and ZX. As per the notation in Fig. 3, setup Y produces a flexural crack perpendicular to the Y-axis, setup Z produces a flexural crack perpendicular to the Z-axis and setups X and ZX produce cracks perpendicular to the X-axis starting from the bottom and the side of the sample, respectively. These results reveal a similar average flexural behaviour of cracking planes perpendicular to the X-axis (setups X with 8.33 MPa and ZX with 8.78 MPa) and Y-axis (setup Y with 8.14 MPa). They all contrast drastically with the average flexural strength measured in cracking planes perpendicular to the Z-axis (setup Z with 4.12 MPa). These findings reveal a significant anisotropy of the flexural behaviour of the 3d printed specimens. The angle between the interlayer interface and the cracking plane seemed to affect the crack formation and progression, ultimately affecting the flexural behaviour. Specimens where the crack cross multiple adjacent layers (setups X, Y and ZX) are significantly less affected by the interlayer bond than specimens where the crack can potentially progress between adjacent layers (setup Z). Hence, the former show higher flexural strength than the latter.

Fig. 9b shows the compressive strength results. The loading direction adopted for the compressive tests was the same as for the flexural ones (i. e., specimens in setups X and Y received compression load perpendicular to the printing layers while specimens in setups Z and ZX received compression load parallel to the layers). Notice that specimens loaded perpendicular to the layer showed an average compressive strength of 47.14 MPa for setup X and 45.79 MPa for setup Y. By contrast, specimens loaded parallel to the layer showed an average compressive strength 33.20 MPa for setup Z and 33.71 MPa for setup ZX. The explanation for the 40% higher compressive strength observed when loading perpendicular to instead of parallel to the layers is again a consequence of the influence of the interlayer bond on the crack formation and evolution. In the first group (i.e., perpendicular), the cracks preferentially go across multiple layers and have less chance of progressing through the interfaces. In the second group (i.e., parallel), the cracks can progress through the interlayer area, being significantly more affected by the weaker interface bond (see Fig. 9b). This denotes a significant anisotropy in the compressive behaviour of the printed material. Despite the differences, most compressive strength values were at or above 30 MPa, which complies with mechanical requirements for structural applications according to the Spanish Structural Concrete Code EHE-08 [27].

The flexural residual performance of the beams is also affected by the differences in cracking formation and propagation observed in the setups. Fig. 10 shows the relationship between the maximum equivalent flexural tensile stress calculated by making a linear-elastic analogy with an uncracked cross-section and the crosshead displacement measured during the tests. Interestingly, beams with flexural cracking planes perpendicular to the printing layers (setups Y and ZX) withstand load for significant deflection increments after the cracking formation. Conversely, beams with flexural cracking planes parallel to the printing layer (setup Z) present negligible post-cracking strength. Such outcome cannot be justified by the influence of the interlayer bond as in previous instances, as the fibres are responsible for providing the residual flexural strength to the beams. The results indicate a strong preferential fibre orientation parallel to the printing layer due to the manufacturing process.

To understand the influence of the curing methods, one of the beams cut from the printed specimen was cured in a curing chamber (according to the description in 'Materials, mixes and production'), and another one was immersed in a water tank for the same period. Fig. 11 presents the flexural and compressive strengths for various batches (with low and intense compaction energy, different cutting and loading directions – test setup – and cement content). The results do not show any trend that could suggest that one curing method yields better mechanical performance than the other. Instead, the differences observed respond to variations in the density of the specimens as a result of the variability of the production process (see Table 3).

Fig. 12 shows the strong correlation between the density and the flexural and compressive strengths, which increase with the density. The analysis of the results for the metallic fibres indicates that the layer thickness and the compaction energy, which directly affect the density of the matrix, are the key variables influencing the mechanical performance of the beams.

Fig. 13 shows the relationship between the average flexural and compressive strengths of mixes with different fibre types that shared the same cement content, layer thickness and compaction energy. Note that the contents of fibres by volume are 1.3% for M, 1.0% for P9, 1.3% for P12, 1.0% for A12 and 1.8% for A22.

The metallic fibres [M] outperform the polypropylene [P] and PVA [A] fibres with equal or higher fibre content (i.e., P12 and A22). The average flexural strength of the beams M is 35% higher than that of the beams P12 and 87% higher than that of beams A22. In terms of the compressive strength, the beams M exhibit values on average 110% higher than those of P12 and 79% higher than those of A22. These results are, in part, explained by the bigger confinement offered by the
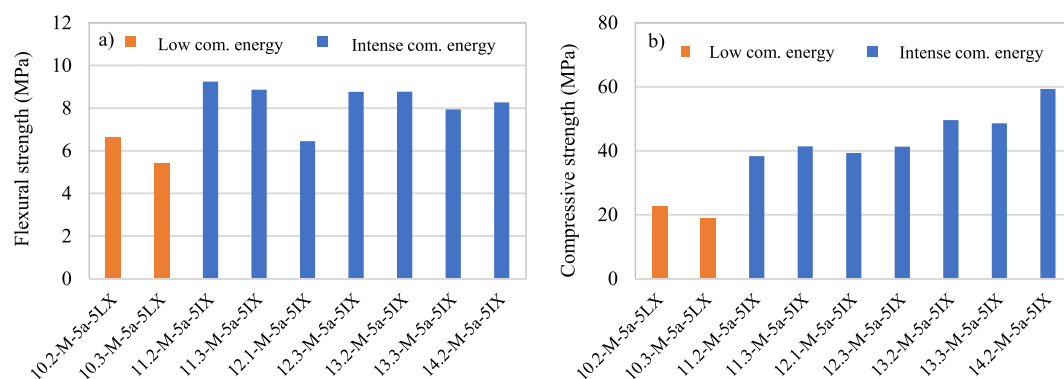

Fig. 8. Influence of compaction energy on a) flexural and b) compressive strengths at 28 d.
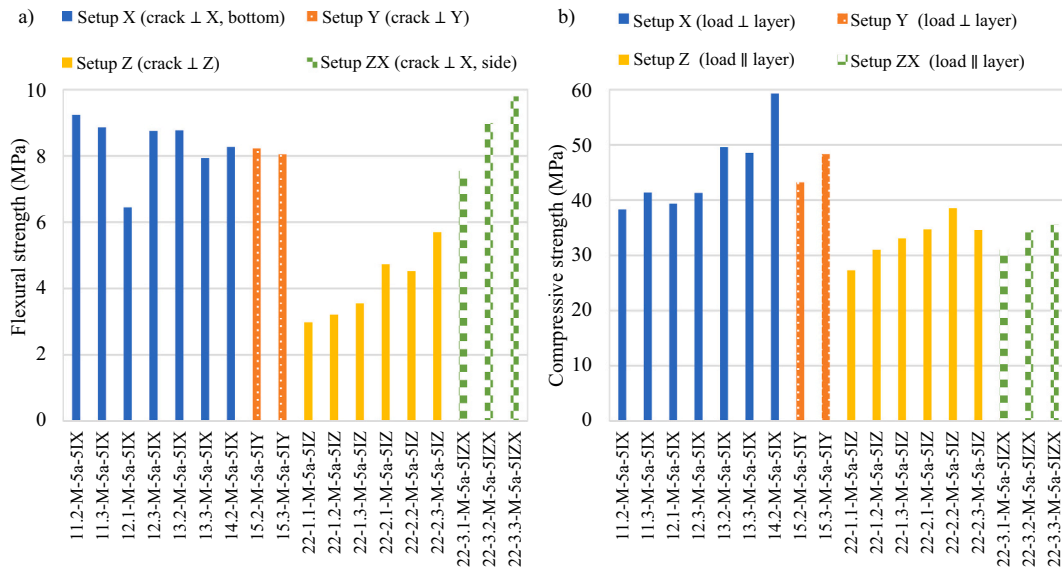
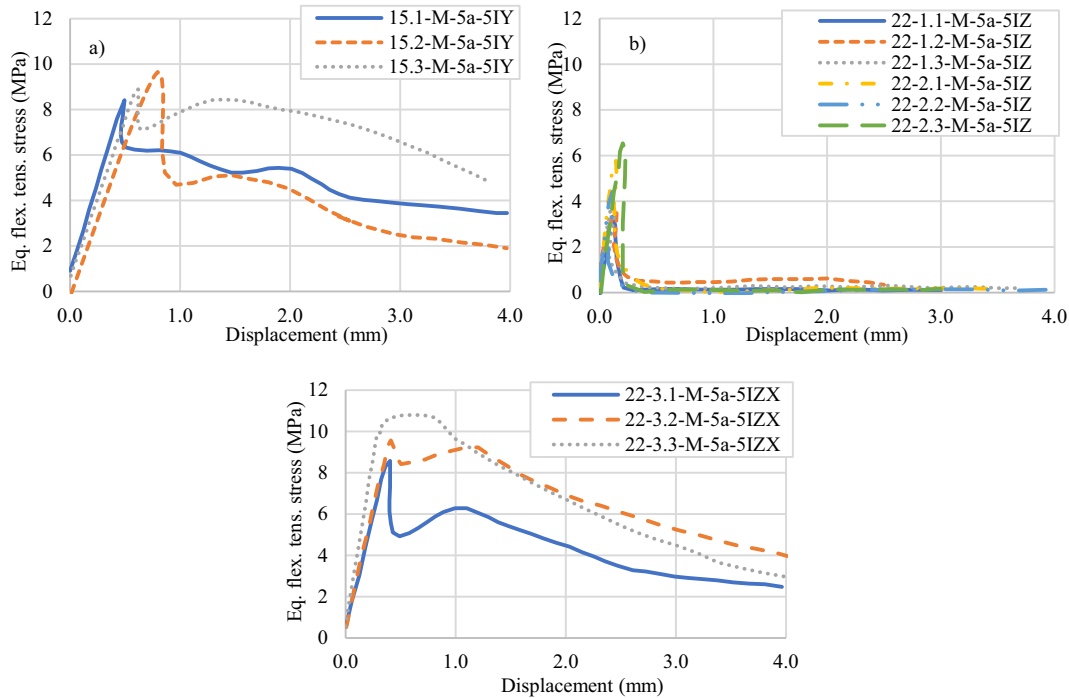**Fig. 9.** Influence of cutting direction on a) flexural and b) compressive strength at 28 days.

Fig. 10. Relationship between equivalent flexural tensile stress and crosshead displacement for setups a) Y, b) Z, and c) ZX.

metallic fibre due to their bigger elastic modulus, which leads to a compressive strength increase of the printed elements (the confinement provided by [P] and [A] fibres should be weaker due to the lower elastic modulus of these fibres). Another aspect that might explain these results is the tendency of PVA fibres (A) to agglomerate during the printing process.

Table 4 presents the modulus of elasticity obtained from three specimens (loaded in the X-axis, perpendicular to the layers). The results indicate an average secant modulus of 4165 MPa. The differences observed among the values of the samples are attributed to the variation in density and compaction of the layers.

The values reported in Table 4 are low (5–6 times) if compared to those of traditional concrete mixes with fibres, which are close to 25,000 MPa. Therefore, structures made with this material should be

more deformable. This higher deformability could be counteracted by stiffening local areas of the structure that govern its overall movement without compromising the sustainability (cost, environmental, and social impacts) [28–32]. This stiffening process can be dealt with from an optimisation perspective using topological approaches [33] leveraging the freedom of shapes the particle bed system can produce.

6. Full-scale particle bed system

Following the development of the material with a small-scale particle bed system, the solution was upscaled to a real-scale printer (see Fig. 19) with a capacity to produce elements with dimensions 2x2x2 m. The same parts, mechanisms and processes found in the small-scale printer were replicated in the large-scale version with the addition of an
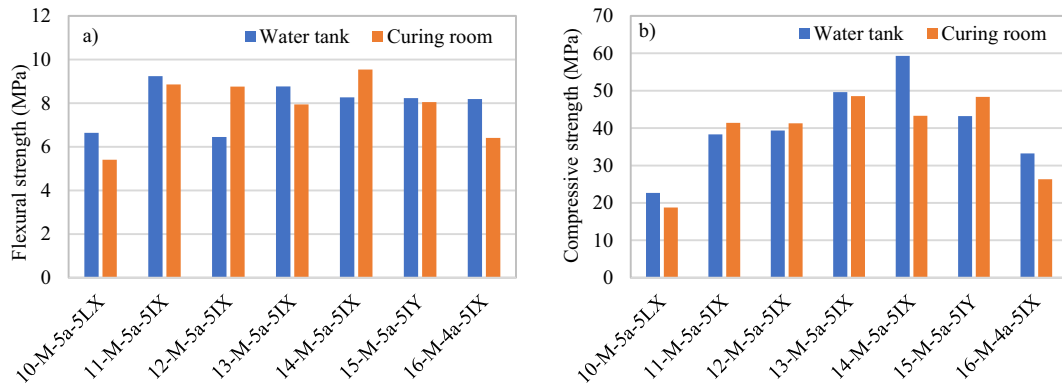
Fig. 11. Influence of curing conditions on a) flexural and b) compressive strength at 28 days.
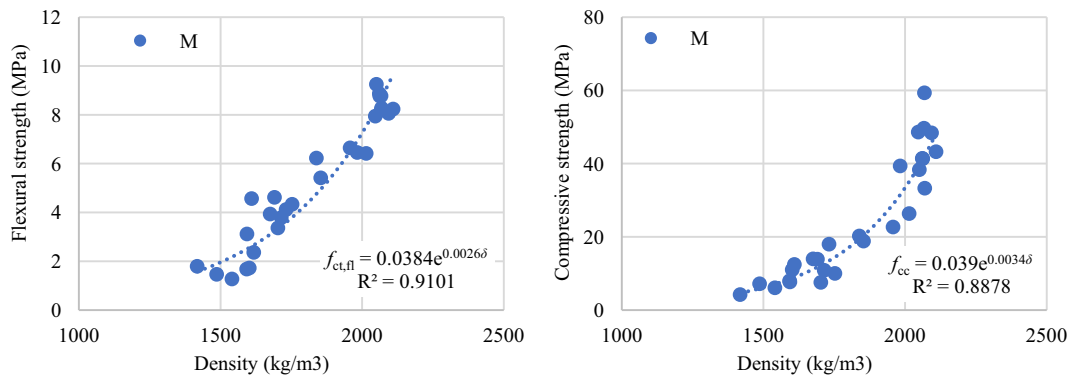

Fig. 12. Correlation between the oven-dry density (δ) and a) flexural ($f_{ct,fl}$) and b) compressive (f_{cc}) strengths at 28 days.
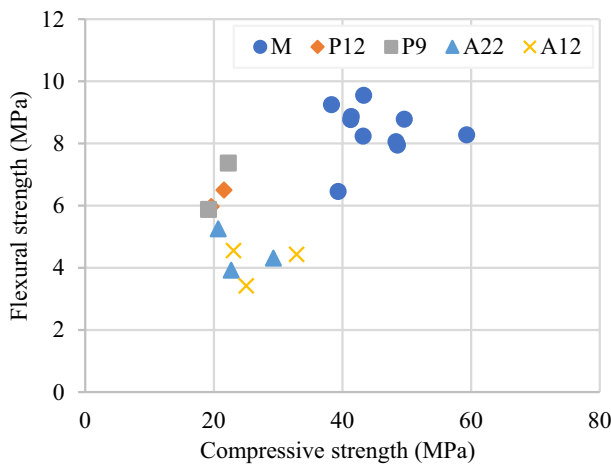

Fig. 13. Relationship between flexural and compressive strengths depending on the fibre type and dosage at 28 days.

Table 4
Modulus of elasticity (E_{cs}).

Specimen	Oven-dry density (kg/m^3)	E_{cs} (MPa)	Average E_{cs} (MPa)
M1	2052	4090	4165
M2	2101	4380	
M3	2042	4024	

automated roller to apply the compaction over the printed material. The roller applied a constant weight to the printed layer as it rolled over it. With a few exceptions, no lifting or dragging of material was observed during the compaction process. Sensors and dedicated software were used to control the printing process.

Several trials were performed to test the nozzles and the flowmeter and evaluate the influence of the pressure in the results as it was expected variations could occur due to the large size of the print head. The experiment involved placing containers over the printing bed to collect the water injected by specific injectors. Furthermore, to evaluate the influence of the position when the injectors are kept open throughout the process, 9 injectors equally spaced alongside the print head injected water while the print head moved (1 is the closest and 9 is the farthest from the system that feeds the print head). To evaluate the influence of selectively opening or closing some of the injectors as the printing head moves, a triangular injection pattern was executed in the 2 directions shown in Fig. 14.

Fig. 15 shows the water volume output for each of the nine injectors for different pump pressures and the relationship between pressure and volume of water. The results show an increase in the volume of water with the pump pressure (see Fig. 15a) and a strong correlation between both parameters (see Fig. 15b). In general, a gradual reduction of the volume occurs with the distance from the system that feeds the printing head. Variations of up to 20% in the water volume output were observed between injectors 1 and 9 due to the head loss experienced due to the long distance the water needs to travel from 1 to 9.

Fig. 16 shows the water collected while selectively opening and closing injectors. An even more pronounced variation in water output was observed in this case. The water output reduces by up to 2.1 times as the injectors close or open, which would equate to change of up to 110% change in the water/cement ratio between areas with the highest and smallest water output and would lead to significant variability in the
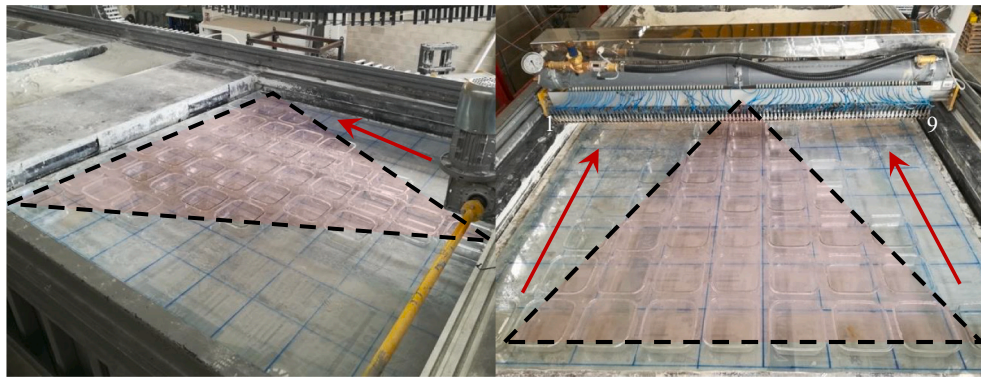

Fig. 14. Trials to assess consistent injection of activator: a) opening and b) closing the injectors in a triangular pattern.

Pressure in mbar — 100, 150, 200, 250, 290, 300
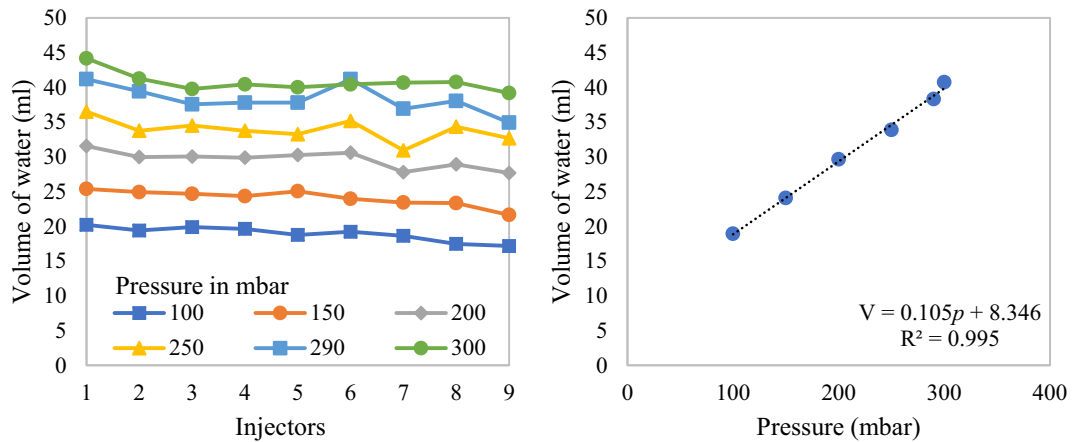
$V = 0.105p + 8.346$
$R^2 = 0.995$

Fig. 15. a) Volume (V) of water injected for different pressures and b) relation between the average volume of water and pressure [P] when injectors are kept open.
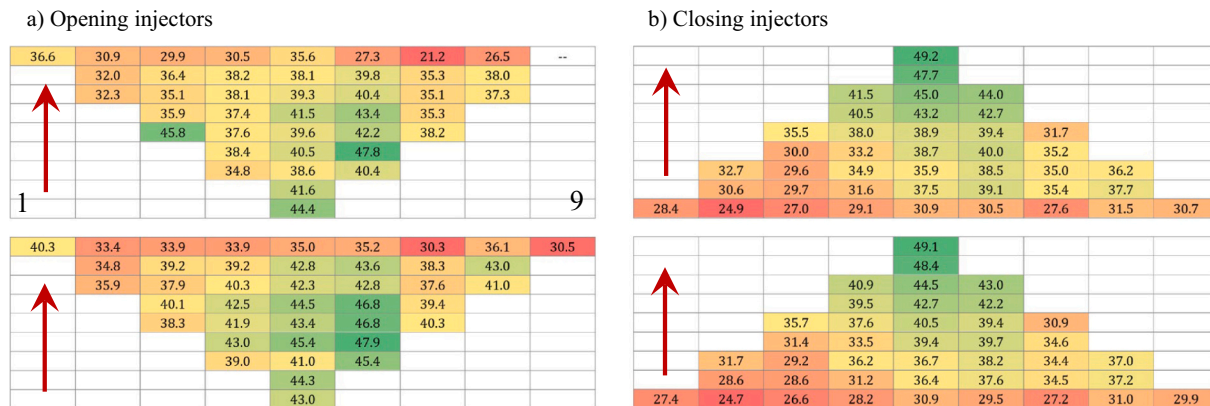
a) Opening injectors

36.6	30.9	29.9	30.5	35.6	27.3	21.2	26.5	--
	32.0	36.4	38.2	38.1	39.8	35.3	38.0	
	32.3	35.1	38.1	39.3	40.4	35.1	37.3	
		35.9	37.4	41.5	43.4	35.3		
		45.8	37.6	39.6	42.2	38.2		
			38.4	40.5	47.8			
			34.8	38.6	40.4			
1				41.6				9
				44.4				

40.3	33.4	33.9	33.9	35.0	35.2	30.3	36.1	30.5
	34.8	39.2	39.2	43.6	43.6	38.3	43.0	
	35.9	37.9	40.3	42.3	42.8	37.6	41.0	
		40.1	42.5	44.5	46.8	39.4		
		38.3	41.9	43.4	46.8	40.3		
			43.0	45.4	47.9			
			39.0	41.0	45.4			
				44.3				
				43.0				

b) Closing injectors

					49.2				
					47.7				
				41.5	45.0	44.0			
				40.5	43.2	42.7			
			35.5	38.0	38.9	39.4	31.7		
			30.0	33.2	38.7	40.0	35.2		
		32.7	29.6	34.9	35.9	38.5	35.0	36.2	
		30.6	29.7	31.6	37.5	39.1	35.4	37.7	
28.4	24.9	27.0	29.1	30.9	30.5	27.6	31.5	30.7	

					49.1				
					48.4				
				40.9	44.5	43.0			
				39.5	42.7	42.2			
			35.7	37.6	40.5	39.4	30.9		
			31.4	33.5	39.4	39.7	34.6		
		31.7	29.2	36.2	36.7	38.2	34.4	37.0	
		28.6	28.6	31.2	36.4	37.6	34.5	37.2	
27.4	24.7	26.6	28.2	30.9	29.5	27.2	31.0	29.9	

Fig. 16. Volume (in cm^3) of water injected following a triangular selective pattern: a) opening and b) closing the injectors.

mechanical performance at different position of the same printed part. The head loss created in the feeding system as the injectors open or close is the main cause of the variations observed. An increase in the number of active injectors might lead to localised pressure and water supply reductions.

The behaviour reported in this section was not observed in the lab-scale prototype due to the smaller size of the printer and the number of injectors, which made it less likely to suffer from significant head loss while printing. Clearly, the direct upscaling of the printing system was not able to cope with the production of bigger parts on an industrial scale. Upon identifying the issue, modifications in the injectors and feeding system were implemented to ensure an output variability below 5% across the printable surface.

Tests were performed -starting from the mix composition 15.2-M-5a-5IY- to evaluate the mechanical performance of 100-mm cubic specimens produced with the large-scale printer. Fig. 17 shows the relationship between the compressive strength (load applied orthogonally to the printing surface) at 28 days and the density obtained for all mix compositions and different compaction levels. The overall trend is similar to the small-scale laboratory tests (see Fig. 12b), although comparatively smaller strength values are obtained for the same density ranges. For the design of structural components, these results were
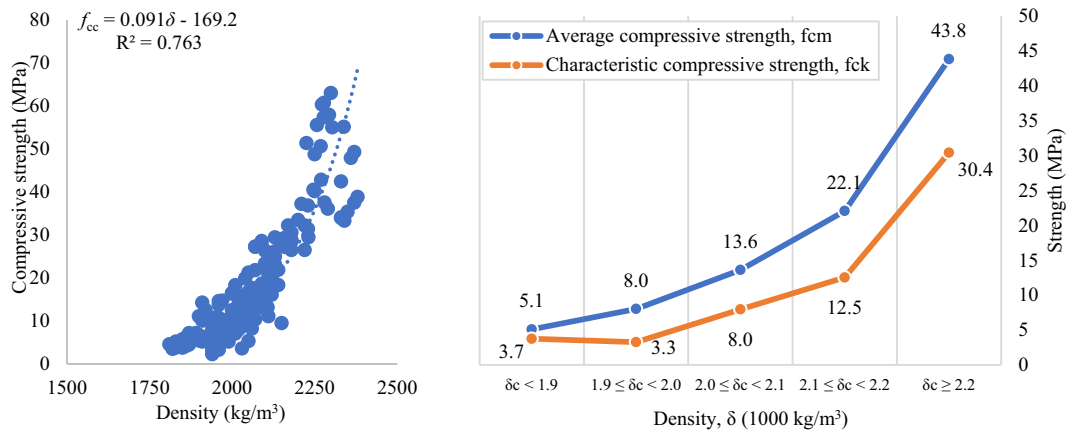
Fig. 17. a) Relationship between compressive strength (28 days) and density for specimens produced with large-scale printer and b) reference average and characteristic values for design.

translated on reference values of average and characteristic (5% fractal) strength values depending on the density achieved during the printing process, as shown in Fig. 17. Notice that minimum densities of 2100 kg/m^3 are needed to achieve strength values compatible with typical structural applications according to design codes.

7. 3DP footbridge in Madrid

In December 2016, a 12.0 m–span arched footbridge made of 3D printed steel microfibre reinforced mortar was open to service in the Parque de Castilla (a public park located in Alcobendas, Madrid, Spain). To the authors' best knowledge, this was the first large structural application of an asset manufactured with the particle bed system based on a selective activation approach for cement-based composites.

The Catalan Institute of Advanced Architecture (IAAC) designed the footbridge following a topological optimisation that minimised the material consumption and the magnitude of the tensile stresses of the cross-section components [19]. The material was developed and characterised by the Polytechnic University of Catalonia (UPC Barcelona-TECH), as described previously. ACCIONA S.A led the production of the footbridge components and their installation. The components were produced at the ACCIONA S.A. facilities in Torrejón de Ardoz (Madrid) using a particle bed system based on the D-Shape® system developed by Enrico Dini in 2013 [11,18,34].

Fig. 18. a) Curing in the temperature-controlled chamber, b) transport of a segment to the external yard, c) curing at external yard environmental conditions, and d) 4-point lifting of the segments with a crane (a red arrow indicates printing direction). (For interpretation of the references to colour in this figure legend, the reader is referred to the web version of this article.)

The footbridge consists of eight U-shaped cross-section segments of steel microfibre reinforced mortar. The microfibres (cold-drawn steel with 3000 N/mm^2 of yield strength) were used to control early and drying shrinkage-induced cracks due to the high cement content and the internal restraints associated with the complex geometry. A single segment was cast per production cycle, which entailed an additional curing stage in a temperature-controlled chamber (see Fig. 18a) to ensure adequate hydration of the external layers of the segment. After the curing, the segments (~1.70 Tons each) were transported with a forklift (see Fig. 18b) to the yard and supported in a metallic platform to minimise bending forces and dynamic effects that could induce cracking.

The segments were stored in a yard (Fig. 18c) for one month. Steel ties were anchored between the webs to prevent failure due to wind gusts or deformations caused by differential heating (i.e., solar radiation). Once the material reached the target compressive strength (>25 N/mm^2), the segments were lifted (Fig. 18d) from four points and placed onto a curved steel frame (Fig. 19a).

The steel frame was used as temporary support to seal the shear joints and the finishing operations (i.e., surfaces smoothing and painting). This frame was later embedded into the final structure (Fig. 19b), thus contributing to the global load-carrying capacity of the footbridge. Note that this was unnecessary from the structural point of view since the 3D printed structure could resist the service loads. Nonetheless, it was deemed convenient to increase the global safety factor of the structure considering the (1) lack of knowledge on the long-term response of the 3DP cement-based composite; (2) novelty of this application and lack of regulations/standards and (3) detrimental economic and reputational impacts a failure of this first application could have for the company and the technology.

The footbridge weighing approximately 15 tons was then transported and placed onto abutments using a single crane in <24 h (see Fig. 20a). Fig. 20b shows a frontal view after installation. The footbridge has been open to the public since December 2016. No structural damage or unacceptable deformations were reported so far. However, shrinkage-induced cracks (with widths <0.2 mm) were observed.

8. Conclusions and recommendations

An extensive experimental program was performed to develop a fibre-reinforced cement-based composite to produce structural components with a particle bed system. Several mix compositions were used in a small-scale particle bed printer and tested under laboratory conditions. The impact of material (fibre type and amount, and water/cement ratio) and production (layer thickness, compaction level, curing conditions, and binding water temperature) parameters on the mechanical performance and density were assessed.

The results helped accelerate the upscaling process that led to the construction of the ACCIONA's footbridge. For this purpose, several technical modifications were carried out on the existing particle bed system (particularly in the printing head) to enable adequate control and quality of large structural segments. The footbridge was placed at the Castilla Park (Alcobendas, Madrid) and remains in service, fulfilling all ultimate and serviceability limit state requirements defined for this structural typology.

The following conclusions were derived regarding the particle bed 3D printing system studied here.

- Contrary to the common knowledge in traditional cast concrete, the addition of fibres produces a significant compressive strength increase in the printed parts. This may be attributed to the extra internal confinement provided by the fibres and the bridging effect of adjacent layers, which should be more pronounced as the fibre elastic modulus increases.
- 3D printed parts can have significant anisotropy in bending and compression due to the weak bond between layers. Strength values can be several times smaller when internal stresses are applied perpendicularly to the printing layers instead of parallel. This should be considered in structural applications to avoid creating weak failure planes.
- An exponential relationship was observed between compressive strength and density of specimens produced with the small- and large-scale printers. As observed elsewhere in the literature, a reduction of the layer thickness and an increase of the compaction energy leads to mechanical performance improvements of the 3D printed specimens. Curves relating to these properties are a simple tool to aid the design of 3D printed parts.

The following recommendations were derived from the findings and observations from the small- and large-scale printers.

- Oven dry densities of >2100 kg/m^3 after printing and the addition of fibres are recommended for elements with serious structural responsibility. Achieving high densities and consistent fibre

Fig. 19. a) Segments supported onto the curved steel frame and b) painted footbridge with the steel frame already embedded.

Fig. 20. a) Support and levelling operations of the footbridge and b) frontal view of the footbridge after installation.

distribution has proven more challenging in the large-scale printer than in the small-scale one. Given the relationship between compressive strength and density, the final density became the reference property for the quality control of the large-scale printing process regarded the water-cement ratio was kept constant.

- The uniformity of characteristics throughout the whole printed surface should be verified in large-scale printers. As shown in this study, the direct upscaling of small-scale setups deployed in the laboratory might lead to significant variations in the distribution of liquid activator, hence not satisfying the quality control and consistency of properties required in a structural part.

CRediT authorship contribution statement

Albert de la Fuente: definition, conceptualization, methodology, investigation, resources, data curation, writing original draft/review, supervision, funding acquisition.

Ana Blanco: validation, investigation, writing-original draft/review, visualization.

Eduardo Galeote: validation, investigation, writing-original draft/review, visualization.

Sergio Cavalaro: definition, conceptualization, methodology, investigation, data curation, writing original draft/review, supervision.

Declaration of competing interest

The authors declare the following financial interests/personal relationships which may be considered as potential competing interests:

Albert de la Fuente Antequera reports financial support was provided by Acciona. Albert de la Fuente Antequera reports a relationship with Polytechnic University of Catalonia that includes: consulting or advisory. Enrico Dini has patent licensed to 8337736.

Acknowledgments

References

[1] M. Pan, T. Linner, W. Pan, H. Cheng, T. Bock, A framework of indicators for assessing construction automation and robotics in the sustainability context, J. Clean. Prod. 182 (2018) 82–95, https://doi.org/10.1016/j.jclepro.2018.02.053.

[2] H. Kloft, H.-W. Krauss, N. Hack, E. Herrmann, S. Neudecker, P.A. Varady, D. Lowke, Influence of process parameters on the interlayer bond strength of concrete elements additive manufactured by shotcrete 3D printing (SC3DP), Cem. Concr. Res. 134 (2020), 106078, https://doi.org/10.1016/j.cemconres.2020.106078.

[3] N. Zhang, M. Xia, J. Sanjayan, Short-duration near-nozzle mixing for 3D concrete printing, Cem. Concr. Res. 151 (2022), 106616, https://doi.org/10.1016/j.cemconres.2021.106616.

[4] S. Bhattacherjee, A.S. Basavaraj, A.V. Rahul, M. Santhanam, R. Gettu, B. Panda, E. Schlangen, Y. Chen, O. Copuroglu, G. Ma, L. Wang, M.A. Basit Beigh, V. Mechtcherine, Sustainable materials for 3D concrete printing, Cem. Concr. Compos. 122 (2021), 104156, https://doi.org/10.1016/j.cemconcomp.2021.104156.

[5] Z. Li, G. Ma, F. Wang, L. Wang, J. Sanjayan, Expansive cementitious materials to improve micro-cable reinforcement bond in 3D concrete printing, Cem. Concr. Compos. 125 (2022), 104304, https://doi.org/10.1016/j.cemconcomp.2021.104304.

[6] T. Marchment, J. Sanjayan, Bond properties of reinforcing bar penetrations in 3D concrete printing, Autom. Constr. 120 (2020), 103394, https://doi.org/10.1016/j.autcon.2020.103394.

[7] V.C. Li, F.P. Bos, K. Yu, W. McGee, T.Y. Ng, S.C. Figueiredo, K. Nefs, V. Mechtcherine, V.N. Nerella, J. Pan, G.P.A.G. van Zijl, P.J. Kruger, On the emergence of 3D printable engineered, strain hardening cementitious composites (ECC/SHCC), Cem. Concr. Res. 132 (2020), 106038, https://doi.org/10.1016/j.cemconres.2020.106038.

[8] C. Esposito Corcione, E. Palumbo, A. Masciullo, F. Montagna, M.C. Torricelli, Fused deposition modeling (FDM): an innovative technique aimed at reusing Lecce stone waste for industrial design and building applications, Constr. Build. Mater. 158 (2018) 276–284, https://doi.org/10.1016/j.conbuildmat.2017.10.011.

[9] A. Perrot, D. Rangeard, E. Courteille, 3D printing of earth-based materials: processing aspects, Constr. Build. Mater. 172 (2018) 670–676, https://doi.org/10.1016/j.conbuildmat.2018.04.017.

[10] R.A. Buswell, W.R.L. da Silva, F.P. Bos, H.R. Schipper, D. Lowke, N. Hack, H. Kloft, V. Mechtcherine, T. Wangler, N. Roussel, A process classification framework for defining and describing digital fabrication with concrete, Cem. Concr. Res. 134 (2020), 106068, https://doi.org/10.1016/j.cemconres.2020.106068.

[11] D. Lowke, E. Dini, A. Perrot, D. Weger, C. Gehlen, B. Dillenburger, Particle-bed 3D printing in concrete construction – possibilities and challenges, Cem. Concr. Res. 112 (2018) 50–65, https://doi.org/10.1016/j.cemconres.2018.05.018.

[12] D. Lowke, I. Mai, E. Keita, A. Perrot, D. Weger, C. Gehlen, F. Herding, W. Zuo, N. Roussel, Material-process interactions in particle bed 3D printing and the underlying physics, Cem. Concr. Res. (2022).

[13] D. Lowke, D. Talke, I. Dressler, D. Weger, C. Gehlen, C. Ostertag, R. Rael, Particle bed 3D printing by selective cement activation – applications, material and process technology, Cem. Concr. Res. 134 (2020), 106077, https://doi.org/10.1016/j.cemconres.2020.106077.

[14] A. Pierre, D. Weger, A. Perrot, D. Lowke, Additive manufacturing of cementitious materials by selective paste intrusion: numerical modeling of the flow using a 2D axisymmetric phase field method, Materials (Basel) 13 (2020) 5024, https://doi.org/10.3390/ma13215024.

[15] J. Ingaglio, J. Fox, C.J. Naito, P. Bocchini, Material characteristics of binder jet 3D printed hydrated CSA cement with the addition of fine aggregates, Constr. Build. Mater. 206 (2019) 494–503, https://doi.org/10.1016/j.conbuildmat.2019.02.065.

[16] G. Ma, R. Buswell, W.R.L. da Silva, L. Wang, J. Xu, S.Z. Jones, Technology readiness: a global snapshot of 3D concrete printing and the frontiers for development, Cem. Concr. Res. (2022).

[17] F.P. Bos, C. Menna, M. Pradena, E. Kreiger, W.R.L. da Silva, A.U. Rehman, D. Weger, R.J.M. Wolfs, Y. Zhang, L. Ferrara, V. Mechtcherine, The realities of additively manufactured concrete structures in practice, Cem. Concr. Res. (2022).

[18] G. Cesaretti, E. Dini, X. De Kestelier, V. Colla, L. Pambaguian, Building components for an outpost on the lunar soil by means of a novel 3D printing technology, Acta Astronaut. 93 (2014) 430–450, https://doi.org/10.1016/j.actaastro.2013.07.034.

[19] IAAC, 3D printed bridge, Institute of Advanced Architecture of Catalonia, 2018. https://iaac.net/project/3d-printed-bridge/.

[20] A. Blanco, P. Pujadas, A. de la Fuente, S. Cavalaro, A. Aguado, Application of constitutive models in European codes to RC–FRC, Constr. Build. Mater. 40 (2013) 246–259, https://doi.org/10.1016/j.conbuildmat.2012.09.096.

[21] P. Pujadas, A. Blanco, S. Cavalaro, A. de la Fuente, A. Aguado, Fibre distribution in macro-plastic fibre reinforced concrete slab-panels, Constr. Build. Mater. 64 (2014) 496–503, https://doi.org/10.1016/j.conbuildmat.2014.04.067.

[22] L. Liao, A. de la Fuente, S. Cavalaro, A. Aguado, Design procedure and experimental study on fibre reinforced concrete segmental rings for vertical shafts, Mater. Des. 92 (2016) 590–601, https://doi.org/10.1016/j.matdes.2015.12.061.

[23] AENOR, UNE-EN 1015-11:2000/A1:2007 Methods of Test for Mortar for Masonry - Part 11: Determination of Flexural and Compressive Strength of Hardened Mortar, 2007.

[24] AENOR, UNE-EN 1015-11:2020 Methods of Test for Mortar for Masonry - Part 11: Determination of Flexural and Compressive Strength of Hardened Mortar, 2020.

[25] AENOR, UNE-EN 12390-13:2014 Testing Hardened Concrete - Part 13: Determination of Secant Modulus of Elasticity in Compression, 2014.

[26] C.M. Boyce, A. Ozel, S. Sundaresan, Intrusion of a liquid droplet into a powder under gravity, Langmuir 32 (2016) 8631–8640, https://doi.org/10.1021/acs.langmuir.6b02417.

[27] CPH, Spanish Structural Concrete Code EHE-08, Comision Permanente del Hormigon, Ministerio de Fomento, Madrid (Spain), 2008.

[28] M. Gebler, A.J.M. Schoot Uiterkamp, C. Visser, A global sustainability perspective on 3D printing technologies, Energy Policy 74 (2014) 158–167, https://doi.org/10.1016/j.enpol.2014.08.033.

[29] S. Ford, M. Despeisse, Additive manufacturing and sustainability: an exploratory study of the advantages and challenges, J. Clean. Prod. 137 (2016) 1573–1587, https://doi.org/10.1016/j.jclepro.2016.04.150.

[30] M. Donofrio, Topology optimization and advanced manufacturing as a means for the design of sustainable building components, Procedia Eng. 145 (2016) 638–645, https://doi.org/10.1016/j.proeng.2016.04.054.

[31] I. Agustí-Juan, G. Habert, Environmental design guidelines for digital fabrication, J. Clean. Prod. 142 (2017) 2780–2791, https://doi.org/10.1016/j.jclepro.2016.10.190.

[32] G. De Schutter, K. Lesage, V. Mechtcherine, V.N. Nerella, G. Habert, I. Agusti-Juan, Vision of 3D printing with concrete — technical, economic and environmental potentials, Cem. Concr. Res. 112 (2018) 25–36, https://doi.org/10.1016/j.cemconres.2018.06.001.

[33] M.A. Meibodi, M. Bernhard, A. Jipa, B. Dillenburger, The smart takes from the strong: 3D printing stay-in-place formwork for concrete slab construction, in: Fabr. 2017, UCL Press, 2017, pp. 210–217, https://doi.org/10.2307/j.ctt1n7qkg7.33.

[34] E. Dini, D-Shape, 2017 d-shape.com (accessed November 1, 2021).